frontiers | Frontiers in Earth Science

TYPE Original Research
PUBLISHED 28 February 2025
DOI 10.3389/feart.2025.1526229

OPEN ACCESS

EDITED BY
Dongri Song,
Chinese Academy of Sciences (CAS), China

REVIEWED BY
Hongzhi Qiu,
Chengdu University, China
Xiaoming Yuan,
Institute of Engineering Mechanics, China Earthquake Administration, China

*CORRESPONDENCE
Kun Liu,
liukun@gsdzj.gov.cn

RECEIVED 11 November 2024
ACCEPTED 10 February 2025
PUBLISHED 28 February 2025

CITATION
Liu K, Wang L, Sun J, Xu S, Lu Y, Tian W and Lu F (2025) Two loess landslide at the same hillslope triggered by the Mw 5.9 Minxian-Zhangxian earthquake in China (July 22, 2013): a comparative analysis of landslide mechanisms.
Front. Earth Sci. 13:1526229.
doi: 10.3389/feart.2025.1526229

Two loess landslide at the same hillslope triggered by the Mw 5.9 Minxian-Zhangxian earthquake in China (July 22, 2013): a comparative analysis of landslide mechanisms

Kun Liu[1,2,3]*, Lanmin Wang[1,2,3], Junjie Sun[4], Shunhua Xu[1,2,3], Yuxia Lu[1,2,3], Wentong Tian[1,2,3] and Fucun Lu[2]

[1]Key Laboratory of Loess Earthquake Engineering, China Earthquake Administration, Lanzhou, Gansu, China, [2]Lanzhou Institute of Seismology, China Earthquake Administration, Lanzhou, China, [3]Gansu Earthquake Agency, Lanzhou, China, [4]College of Civil Engineering and Architecture, Wenzhou University, Wenzhou, China

Strong earthquakes and heavy rainfall are recognized as significant triggers of landslides, where the failure characteristics are intricately controlled by internal geological conditions of the slope. This study focuses on the investigation of two landslides triggered by the 2013 Minxian-Zhangye earthquake (Mw = 5.9, USGS). These landslides occurred on the Wamuchi slope, located approximately 22 km east of the epicenter in Minxian County, Gansu Province. Despite being less than 100 m apart, the two landslides exhibited significantly different flow sliding characteristics.The western landslide had a sliding distance of approximately 1.124 km, resulting in 12 fatalities, while the eastern landslide covered a distance of about 340 m.To further analyze the mechanisms of the two landslides and the reasons behind the differences in their flow sliding characteristics, we conducted field investigations and laboratory tests, including drilling, high-density electrical testing, unmanned aerial vehicle photography, and dynamic triaxial testing. A comparative analysis was performed on the landslide morphology, hydrogeological conditions, topography, and site-specific factors for both landslides.The results indicate that both landslides were triggered by a combination of seismic activity and rainfall. However, differing geological, hydrological, and topographical conditions, as well as site-specific influences, led to distinct mechanisms for each landslide, resulting in significant variations in their sliding characteristics.Understanding the initiation and movement mechanisms of such flowslides on slopes is crucial for effective landslide hazard analysis and mitigation strategies.

KEYWORDS

loess flowslide, combined effects, liquefaction, shattering loess, site effects

1 Introduction

On 22 July 2013, the Minxian-Zhangxian (M-Z) earthquake (Mw = 5.9, U.S. Geological Survey) occurred on the NW-SE trending Lintan-Tanchang fault zone (LTFZ) at the northeastern margin of the Tibetan Plateau in Gansu, China (Figure 1). The strong earthquake left 95 people dead, 2,414 people injured, and an economic loss of more than $5 billion U.S. dollars (Wang L. M. et al., 2017). In total, the earthquake triggered 2,330 landslides, and 600 landslides in the loess deposit (Wang and Wu, 2014; Xu and Sun, 2013; Xu and Sun, 2013).

Among these landslides, two typical flowslides within 100 m of each other occurred at the Wamuchi hillslope located in Yongguang village in Minxian County, Gansu Province (Figure 1). The Western flowslide, a large-scale landslide with an area of 45,200 m^2, was induced in the loess deposit of Q3 and buried almost the entire Wamuchi village, resulting in the deaths of 12 people (Wang L. M. et al., 2017). The displaced mass traveled a distance of 1.124 km and exhibited characteristics typical of a flowslide (Varnes, 1958). The other event, referred to as the Eastern landslide, exhibited a sliding distance of 0.552 km and covered an area of 34,500 m^2. Compared to the western landslide, the eastern landslide has a shorter sliding distance and does not exhibit significant liquefaction

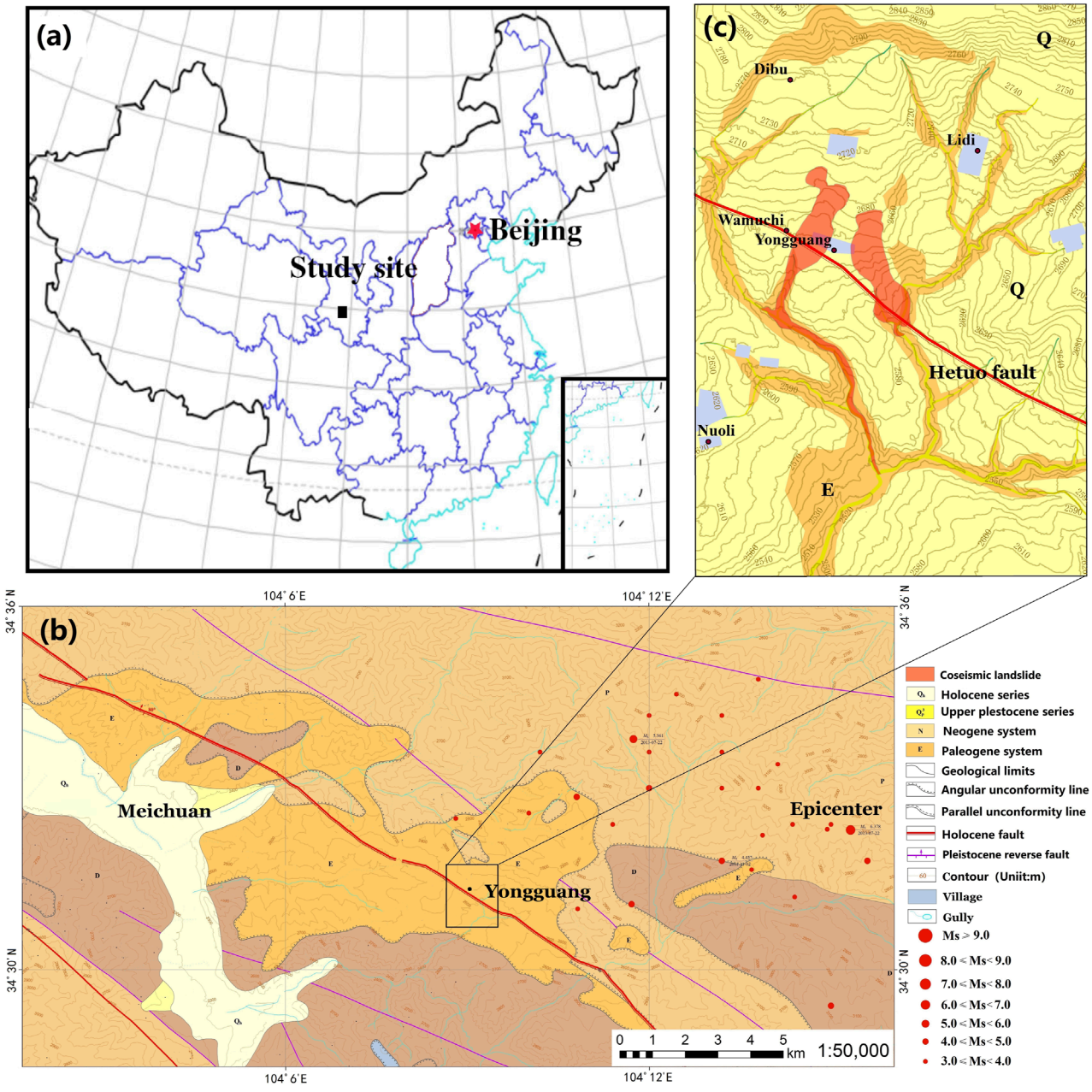

FIGURE 1
Location of the Wamuchi Hillslope **(A, B)** and geological map **(C)**.

features. However, despite being less than 100 m apart, the two landslides show markedly different flow sliding characteristics. It is hypothesized that the variation in hydrogeological conditions is a key factor controlling these differences.The recent loess liquefaction debris flow disaster occurred on 18 December 2023, as a result of the 6.2 magnitude earthquake in Jishishan County, Gansu Province. This typical seismic liquefaction landslide-debris flow was triggered in Jinchuan Village and Caotian Village of Minhe County, Haidong City, Qinghai Province, causing extensive burial of numerous houses under sediments several meters thick (Wang, L et al., 2024). One of the significant external factors contributing to this disaster was prolonged irrigation and three consecutive days of winter irrigation before the earthquake, which led to a rise in the groundwater level (Xu et al., 2024).The natural loess exhibits pronounced structural integrity and favorable vertical stability. However, due to its remarkable hydrosensitivity, significant strength deterioration occurs during moisture absorption processes, resulting in over 90% of loess-related disasters being water-associated (Ma and Peng, 2022). The two disasters in Zhongchuan Township and Yongguang Village share similar external triggering factors: First, Zhongchuan Township had long-term irrigation practices and conducted a 3-day winter irrigation immediately before the earthquake. In contrast, Yongguang Village was in its rainy season before the earthquake and had abundant shallow groundwater (Lu et al., 2024a). Both disasters were closely related to groundwater.Therefore, it is crucial to investigate the correlation between regional hydrogeological conditions and mudflow disasters (Chen, L. et al., 2024).

Because of casualties and severity of the disasters, most attention was paid on the Western flowslide. Loess liquefaction by the earthquake triggered this flowslide, which flowed down the gully for a distance much longer than that of the unliquefied loess (Wang L. M. et al., 2017). The Western flowslide was examined from the point of view of the combined effect of earthquake and rainfall. As a post-earthquake scientific investigation indicated, the water content of the sliding loess here was above the plastic limits (Xu and Sun, 2013). Under the action of earthquake and rainfall, a low-angle, fast and long-distance loess landslide (Western flowslide) occurred, and a fan-shaped accumulation area was formed. Many field investigations, laboratory tests, and analyses were completed by researchers from the Lanzhou Institute of Seismology, China at the Earthquake Administration, including evaluation of the loess site amplification effect based on microtremor measurement (Yan et al., 2013), analysis of strong ground motion (Huang et al., 2013; Tian et al., 2013), estimation of peak ground acceleration in epicentral area (Wang and Liu, 2013), surface wave investigation (Che et al., 2013), loess static and dynamic triaxial tests (Wang Q. et al., 2017), and a survey of the overburden thickness of sites (Li et al., 2018).Wang Q et al. identified the loess characteristics of the Yongguang Village western landslide through field investigations and laboratory triaxial tests, conducting analytical assessments of seismic site response, slope stability, and liquefaction potential (Wang Q et al., 2021). Wang Lanmin et al. developed an experimental model based on the saturated liquefied mudflow of the western surface layer in Yongguang Village and performed shaking table tests to validate the disaster formation mechanism of saturated liquefied mudflows on loess slopes (Wang, L et al., 2023).The groundwater distribution in Yongguang Village was investigated by Lu, F. C. et al., and the landslide susceptibility under rainfall and earthquake-rainfall coupling conditions was calculated based on the TRIGRS model and Scoops 3D model, respectively (Lu et al., 2024b).Due to the uniqueness of the western landslide, numerous scholars have focused primarily on the study of this landslide. However, due to the uniqueness of the western landslide, many researchers have primarily focused on studying this specific landslide, while few have conducted comparative analyses of the landslide morphology, hydrogeological conditions, topography, and site conditions of the two landslides.

Intense ground movements and rainfall infiltration play a crucial role in the triggering mechanisms of landslides. However, it remains challenging to explain why two landslides occurring on the same slope under identical internal and external factors (such as earthquakes and rainfall) exhibit significantly different sliding characteristics. This study conducted a comparative analysis of landslide morphology, hydrogeological conditions, topographic characteristics, and site conditions through comprehensive field investigations and systematic testing, including borehole drilling, high-density resistivity testing, unmanned aerial vehicle (UAV) aerial surveys, and topographic wetness index (TWI) calculations. The research objectives focus on elucidating the controlling factors responsible for the differential flow-slide characteristics and revealing the distinct failure mechanisms between the two landslide cases. This integrated methodological approach enables multi-dimensional characterization of slope instability through the synergistic interpretation of subsurface geotechnical data, surface hydrological parameters, and high-resolution terrain modeling. Notably, from the perspective of hydrological processes, the causation of landslides is still not fully understood, and a definitive triggering mechanism has yet to be proposed.

2 Geological, topographic, tectonic setting, rainfall and ground motion

2.1 Geological, topographic, and structural conditions

According to the active fault survey launched by Earthquake Administration of the Gansu Province and other research (He et al., 2013; Xu et al., 2013; Zheng et al., 2013), the Hetuo fault with which the M-Z earthquake was associated is the secondary fault of the LTFZ, and the Wamuchi hillslope located on its hanging wall (Figure 2).

The tectonic activities and deformation pattern of LTFZ are closely related to northward indentation and eastward movement along the Eastern Kunlun Fault and the Left-lateral slip of the West-Qinling Northern Fault, which contribute to the frequent occurrence of intermediate-strong earthquakes (Zheng et al., 2013). The LTFZ is composed of several secondary faults with different scales or parallel or oblique joints. This outcropping fault mainly thrusts southward and extends northwest-northwest. It tends toward the northEastern with a dip angle of 50–70° locally, steep or southward, and has a left-lateral strike-slip component.

In addition, the LTFZ was formed in the Hercynian period, and more actively in the later tectonic movement, cutting and breaking the strata of different age. On the north side, the Permian

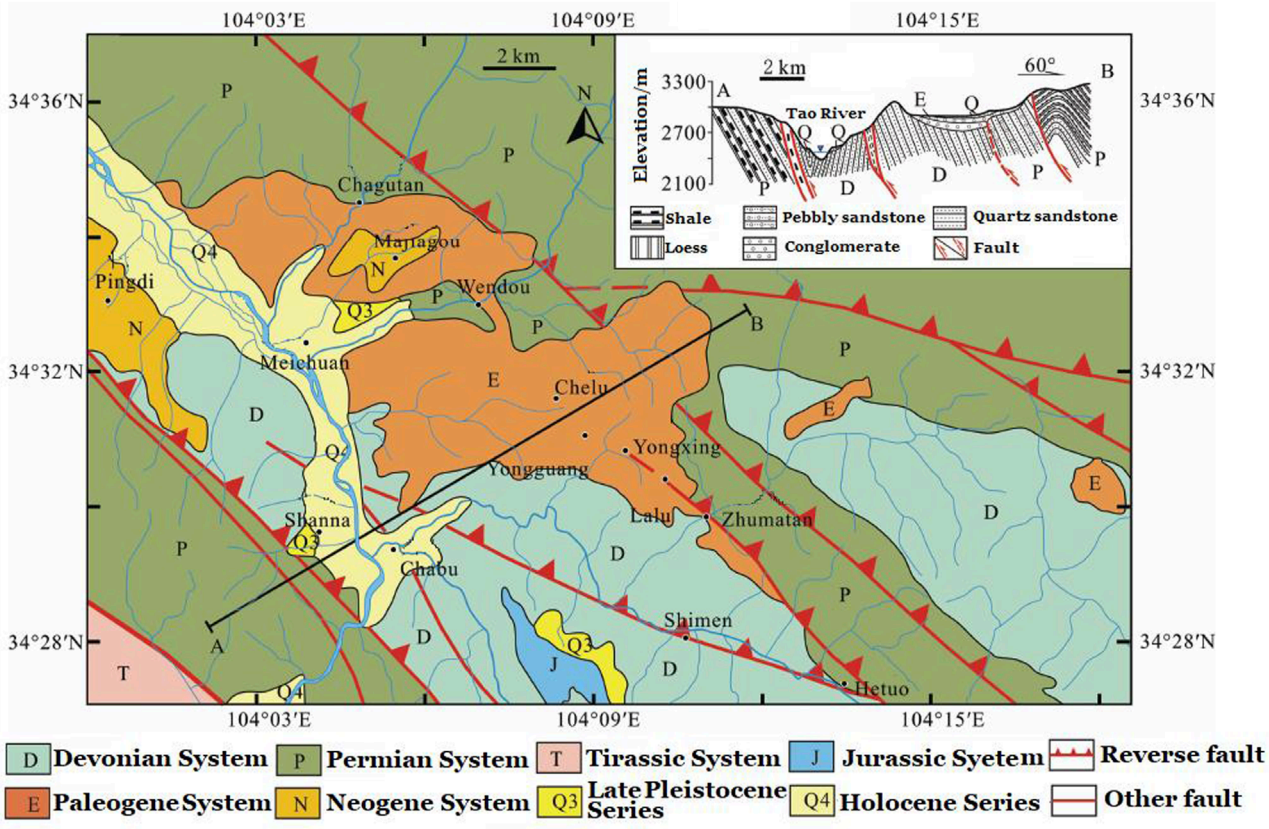

FIGURE 2
The geological map of the LTFZ [Modified from (Zheng et al., 2013)].

slate, sandstone, and mudstone threw southward over the Paleogene conglomerate and sandy conglomerate. The Paleogene sedimentary thickness in the vicinity is obviously thicker, forming a Paleogene basin. Moreover, the Hetuo fault below the Paleogene sedimentary basin trace passes through an accumulation area of the Western flowslide.

The Wamuchi hillslope, located 22 km from the epicenter of the MZ earthquake, is a colluvial fan covered by an aeolian loess in the foothills of the Jingushan mountain (Figure 3). It was strongly incised by the Wamugou and Hongshuigou gully as well as another small gully, forming an independent slope. The pre-earthquake topography of the hillslope indicates that the elevation descended from the north to the south, with the highest point being 2,850 ma.s.l. at the peak of the colluvial fan and the lowWestern point being 2,605 ma.s.l. at the joint of the Wamuchi gully and the Hongshuigou gully. The altitude difference is about 245 m over a horizontal distance of 1.35 km.

The strata in the Wamuchi hillslope are mainly composed of Malan loess formed in Q3, with uneven silty content and thicker overburden (Figure 1). Due to the thrust-nappe effect of the LTFZ, the lithology can be classified into the following: (1) the Paleogene system (N), which consists of the siltstone, silty mudstone with a small amount of shell; and (2) the Upper Pleistocene series (Q), which is dominantly composed of Loess and silt soil.

2.2 Rainfall records

The climate of Minxian County is characterized as semi-humid, with notable rainfall concentrated during the months of July and August. According to rainfall data sourced from the China Meteorological Administration for the period of 2010–2016 at the Minxian rainfall monitoring station located in Awu (approximately 30 km southwest of Wamuchi), the average monthly precipitation in July amounts to approximately 62 mm. Furthermore, based on publicly available reports, the average annual precipitation in Minxian County is recorded at 603 mm.

Records of daily rainfall obtained at the Minxian rainfall base station indicate that between July 1 to 22, 2013, the area received 126.3 mm of rainfall, with the peak daily rainfall of 24.4 mm occurring on July 4 (Figure 4). Records of hourly rainfall obtained from an unattended station at a different distance from the rainfall station to the Wamuchi hillslope indicate that from 8:00 on July 21 to 8:00 on July 22, the accumulative 24-h rainfall in the mountain area was 11–24 mm (Figure 5). The pre-earthquake rainfall process recurred in the pattern of dense multi-day light rain, moderate rain, and independent single-day heavy rainfall. Intensive light rain and moderate rain are favorable for rainfall infiltration, whereas heavy rain has a strong erosion effect on the surface. Thus, the rainfall process before the earthquake not only increased the water content

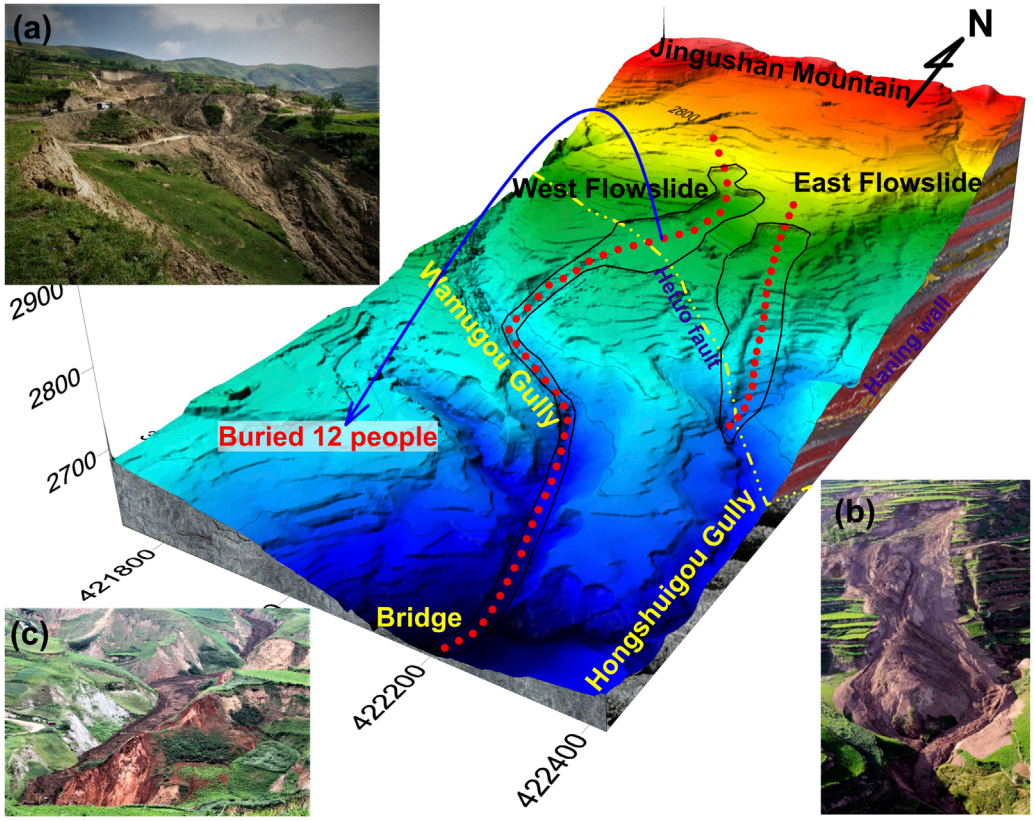

FIGURE 3
Post-earthquake 3D topography models and overview of flowslide. **(A)** View from head scarp to the Western flowslide. **(B)** View from head scarp to the Eastern landslide. **(C)** Sliding zone of the Western flowslide.

of the loess deposit, but it also supplied underground water through the vertical fissures in the deposit.

The average rainfall in the study area for July was 62 mm, while the cumulative precipitation over the 21 days preceding the landslide event (July 1–22) reached 126.3 mm, approximately twice the monthly average. The total precipitation for July 2013 was 218.7 mm, marking the highest monthly rainfall recorded since 1993. This prolonged saturation likely served as a prerequisite condition for the landslide occurrence. Field investigations and laboratory analyses further revealed that the loess soil moisture content increased by 15%–20%, leading to a sharp decline in shear strength (for details on the process, refer to Section 4.3 of this paper).Due to continued rainfall, several much smaller landslides occurred close to the Wamuchi hillslope prior to 22 July 2013. On the day of the landslide, 14.3 mm rain was recorded. By this time, however, the ground was already saturated.

It is worthy to mentione that heavy storms have hit these areas regularly in May–June in recent years. The most damaging of these earlier debris flows, triggered by a rainstorm with 6 h of rainfall totaling 56.8 mm, occurred on 10 May 2012 in the town of Chafu, located about 6 km northWestern of Wamuchi. Forty-five people were killed during the flowslide (Wang, 2014). Two months after the M-Z earthquake, another landslide induced by heavy rain (with a maximum cumulative rainfall of 96 mm) occurred in the Dalong village, located about 3.3 km north of the Wamuchi hillslope.

2.3 Ground motion of the M-Z earthquake

Strong ground shaking from aftershocks following the 2013 M-Z earthquake was recorded by the accelerograph network of the National Strong-Motion Observation Network System of China (NSMONS). Ground motions from the mainshock were observed at 64 stations, with the maximum peak ground acceleration (PGA) of 177 Gal recorded at station 62MXT, located 18 km east of the epicenter and 19 km northeast of the Wamuchi hillslope (Huang et al., 2013). However, no strong ground-motion records are available at the landslide site.

Historically, earthquake intensities were often estimated based on the toppling and sliding of objects such as tombstones before the advent of strong-motion seismographs. In the meizoseismic area affected by the M-Z earthquake, many iron doors with and without brick doorposts provide valuable statistical data for estimating PGA based on doorpost destruction (Wang and Liu, 2013). Estimates suggest that horizontal PGAs in Hetuo, a prominent meizoseismic area, can reach 520–550 Gal, significantly exceeding the reference value for the eighth degree on the Chinese Earthquake Intensity Scale.

Moreover, PGAs are notably higher on the hanging wall of the Hetuo fault. Therefore, proximity to fault features such as the thrust component or being on the hanging wall contributed significantly to the occurrence of landslides.

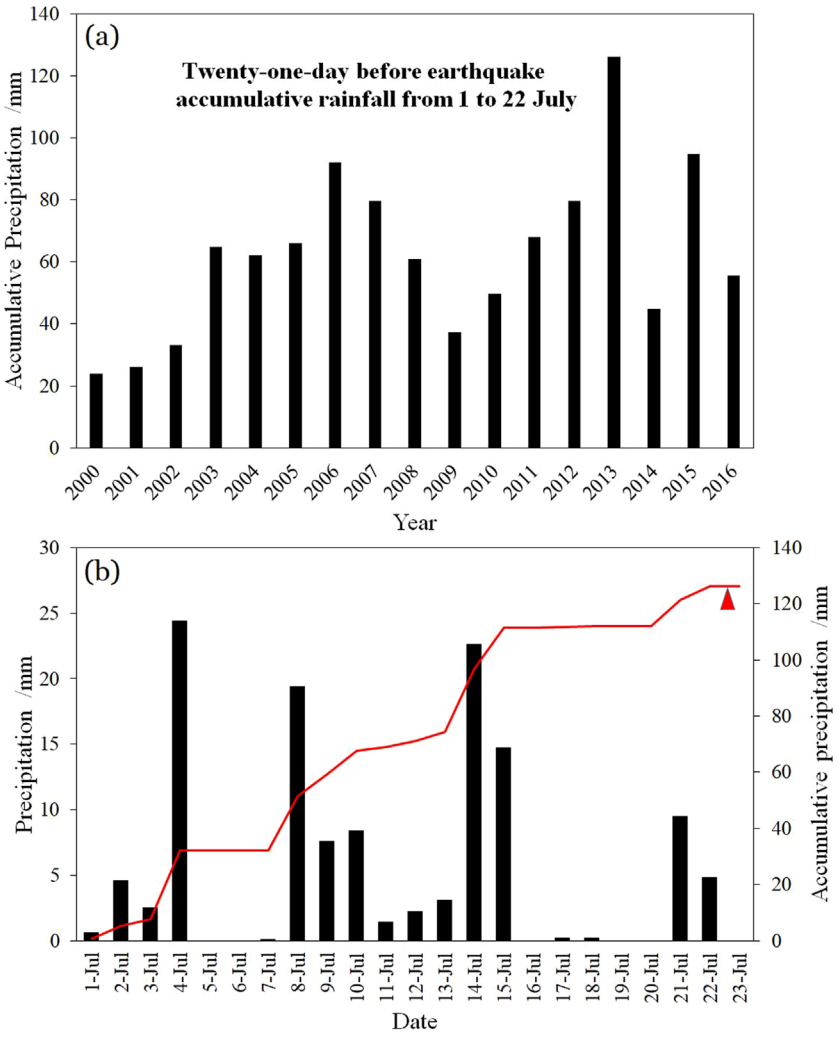

FIGURE 4
Rainfall data of Minxian base station for Minxian County: **(A)** Cumulative precipitation from July 1 to 23, 1990–2000; **(B)** Precipitation from July 1 to 23, 2016; (data from China Meteorological Administration).

3 Methods

The primary triggers for the landslides on the east and west sides of Yongguang Village are the coupling of rainfall and seismic activity. However, under similar rainfall conditions, significant differences in sliding characteristics are observed in soil samples from the same slope body separated by less than 100 m. It is hypothesized that these differences are primarily due to variations in hydrological and geological conditions and the topographical features of the landslides. Therefore, we performed a comparative analysis of the landslide morphological parameters for the east and west landslides and utilized high-density electrical resistivity methods and drilling to investigate the stratigraphic structure and groundwater distribution at both sites. Given that the groundwater recharge in the study area is solely from rainfall, pre-seismic topographic trend analysis and TWI (Topographic Wetness Index) calculations were conducted to assess rainfall runoff conditions and identify areas more affected by rainfall. Additionally, soil samples from the landslide bodies were subjected to loess liquefaction tests to further explore the reasons behind the significant differences in landslide characteristics.

3.1 High-density electrical resistivity method

The electrical conductivity of geological media varies with factors such as the composition and structure of the medium. The high-density resistivity method applies a stable artificial electric field to the geological medium using ground electrodes, observing changes in the electric field and current distribution to analyze the distribution of geological layers or structures and calculate the resistivity of the geological medium. “High-density” refers to the closely spaced electrodes, which enhance operational efficiency and facilitate data processing. This method allows for rapid and accurate analysis of resistivity distribution and cross-sectional features of the geological medium. The principle involves supplying power to any

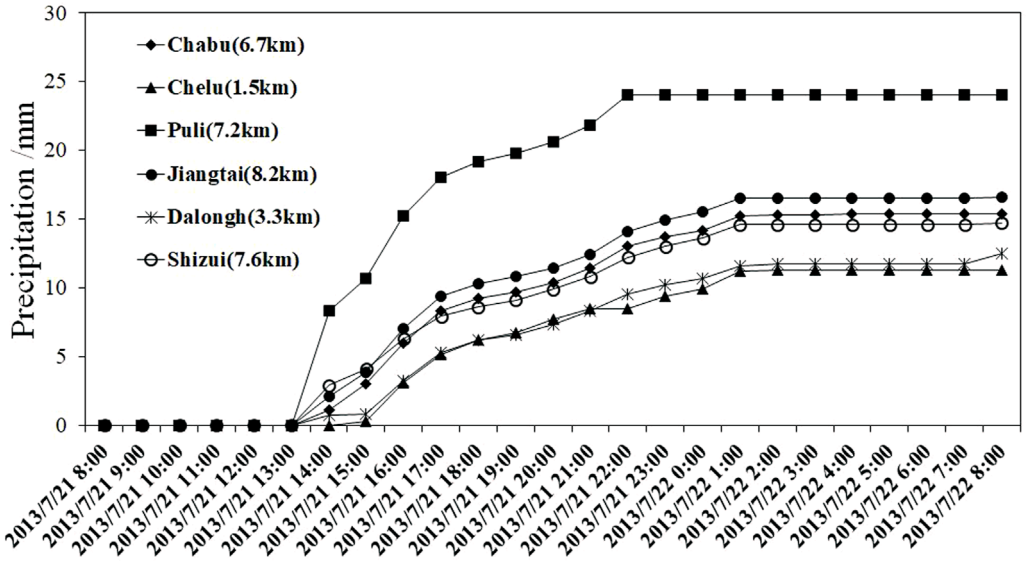

FIGURE 5
Rainfall data of mountain area unattended station for Yongguang village for 24 h before the earthquake (data from Meteorological Administration in Dingxi City).

two points (A and B) on the surface of the target area to create a direct current electric field. The electric potential is then measured between any two other points (M and N) on the surface. Using the principle of linear superposition of direct current electric fields, the potential difference between points M and N can be calculated, and the resistivity of the geologic medium between M and N can be determined by Equations 1, 2:

$$\rho = K\frac{\Delta U_{MN}}{I} \tag{1}$$

$$K = \frac{2\pi}{\frac{1}{AM} - \frac{1}{AN} - \frac{1}{BM} + \frac{1}{BN}} \tag{2}$$

In the formula, K represents the device coefficient for the high-density electrical resistivity method, which describes the physical quantity related to the spatial arrangement of the electrodes.

3.2 Topographic wetness index

The Topographic Wetness Index (TWI) is defined as the natural logarithm of the ratio of the upslope contributing area to the local slope per unit contour length. The concept of TWI was first introduced by Beven and Kirkby (1979) to predict soil moisture content. As a composite topographic indicator, TWI helps identify rainfall runoff patterns, potential areas of increased soil moisture, and water accumulation zones. It is significant for delineating topographic variations, predicting and assessing spatial distribution of moisture, and calculating flow saturation and contributing areas. The formula for TWI is shown in Equation 3:

$$TWI = \ln[SCA/TAN(\text{slope})] \tag{3}$$

where SCA represents the upslope contributing area and slope denotes the local slope.

4 Results and analysis

4.1 Comparison of landslide morphology

The flowslides occurred between 7:45 and 7:50 a.m. local time on 22 July 2013. Initial media reports and research initially categorized the event as a mudslide, mudflow, or loess flow. However, field observations indicate that these landslides are best classified as flowslides (Hungr et al., 2001). The event commenced with the failure of a loess slope, followed by rapid movement along a gully in an extremely swift and voluminous flow-like motion.

The Western flowslide occurred in the lower-middle part of the hillslope and upstream of a small gully, while the Eastern landslide took place at the eastern edge of the hillslope adjacent to the Hongshuigou gully, only 100 m apart but sliding into different gullies (refer to Figure 6).

The Western flowslide exhibited a distinct sliding morphology. In the source area, sliding occurred in two phases: the main slide and a subsequent slide, moving consistently at orientations of 204° SSW and 143° SE, respectively. In the runout zone, the flow pattern resembled an "L" shape, with displaced loess from the Wamuchi landslide source area depositing along previous landslide channels.

Based on accumulation characteristics, the terrain of the Western flowslide along the sliding path can be divided into three sections (Table 1). The first section comprised the upper part of the Western hillslope, with altitudes ranging from 2,764 to 2,731 m above sea level (ma.s.l.) and slope angles of 13°–15°. This section likely experienced historical landslides along the strike of the strata due to its smooth and moderate slope. The second section was a flat area, part of the residential Wamuchi village, with an average slope angle of 4.2° and a height difference of 5 m, descending from 2,727 to 2,722 ma.s.l. The third section included the gully channel,

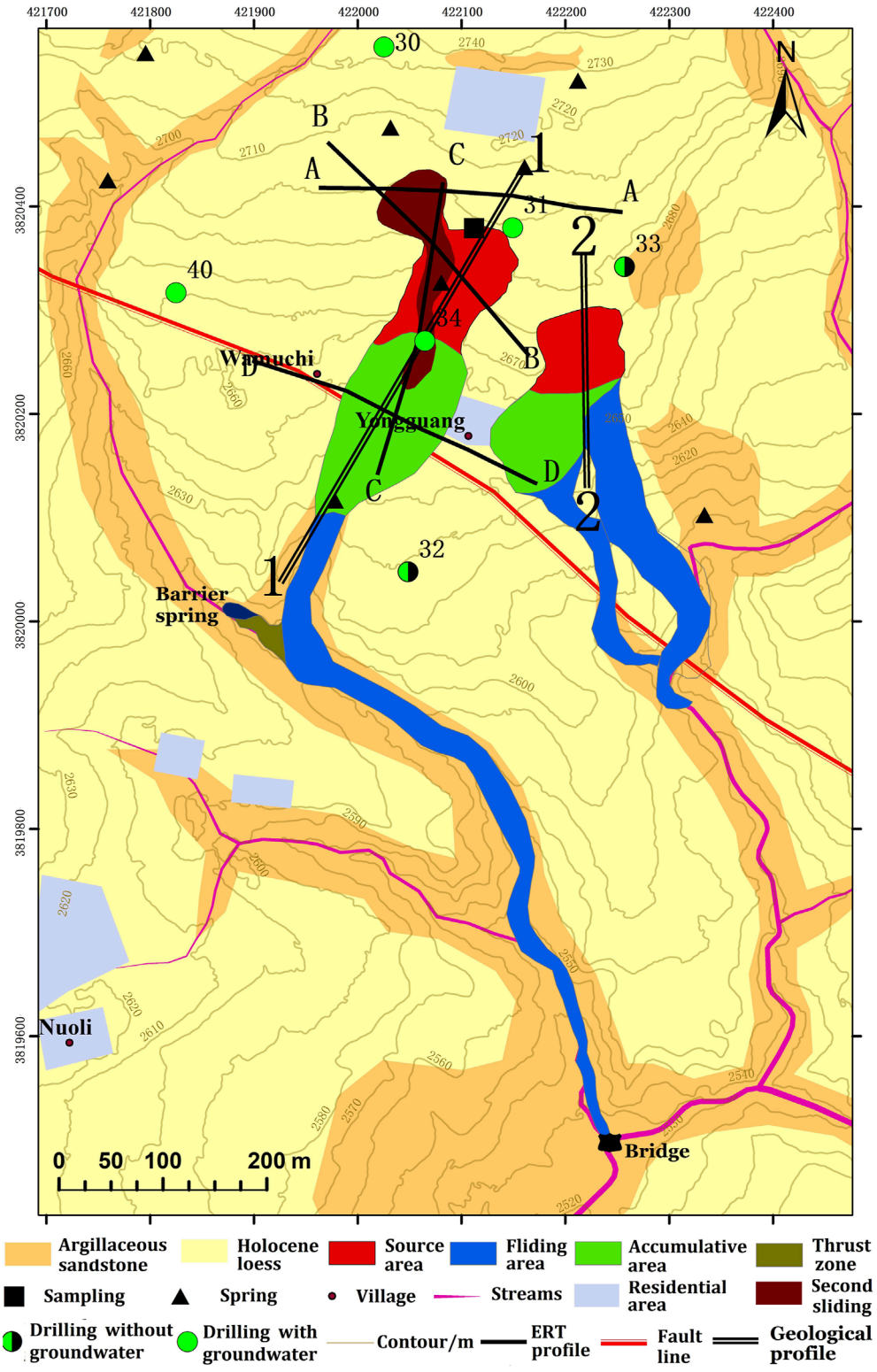

FIGURE 6
Field plan of the geotechnical and geophysical investigations of the two flowslides.

ranging from 2,724 to 2,724 ma.s.l., with slope angles between 6° and 10°, where it converged with the Hongshuigou gully near a stone bridge.

For the Wamuchi landslide, three sections were delineated based on the sliding characteristics. The first section covered the upper part of the Western hillslope, with altitudes ranging from 2,755

TABLE 1 Geometric parameter of the two flowslides.

Zone	Terrain feature	The western flowslide		The eastern Landslide
		Main slide	Second slide	
Source Area	Area/m^2	9,400	3,500	6,000
	Volume/m^3	198,000	3,200	75,000
	Top altitude/m	2,764	2,770	2,755
	Toe altitude/m	2,731	2,754	2,736
	Altitude difference/m	33	16	19
	Length/m	126	68	78
	Direction/°	204	143	195
	Average slope/°	14.6	13.2	13.6
Accumulation Area	Area/m^2	15,900	None	7,200
	Length/m	185		104
	Average thickness/m	12		5
	Average altitude/m	2,725		2,730
	Average slope/°	4.2		7.5
Sliding Area	Area/m^2	16,400	3,170	21,300
	Length/m	745	147	340
	Top altitude/m	2,724	2,754	2,735
	Toe altitude/m	2,607	2,726	2,647
	Altitude difference/m	117	28	88
	Direction/°	162	195	158
	Average slope/°	8.8	10.8	17.4

to 2,736 ma.s.l. and slope angles of 12°–15°. The accumulation area was smaller compared to the Western flowslide, and the sliding path was shorter and steeper than that observed in the Western flowslide.

4.2 Landslide controlling factors analysis

Landslides always occur when the shear stress along a potential sliding surface exceeds the material strength. With respect to rainfall, slope failure is mainly due to a loss in shear strength when soil suctions are decreased by rainfall infiltration in the unsaturated soil or positive pressures are significant built up by a rising groundwater table in the saturated soil. In addition, shear stress along the soil/bedrock interface increases by increasing the pressure head of the rainfall infiltration (Zhang et al., 2011). In relation to earthquakes, liquefaction in the saturated soil or shattering in the unsaturated soil caused by strong ground motion largely reduces the strength of the substrate. In addition, shear stress along the soil/bedrock interface increases when inertia force from strong ground motion is applied. Under the combined effect of rainfall and earthquake, the slope instability mechanism becomes more complex and varied.

For the Western and Eastern landslides that are located within 100 m of each other, the conditions of earthquakes and rainfall were likely similar. When comparing the failure mechanisms of the two flowslides, the geological condition of the slope, such as the terrain and stratum of the slope and the mechanical properties of soil and ground water, were extremely critical controlling factors.

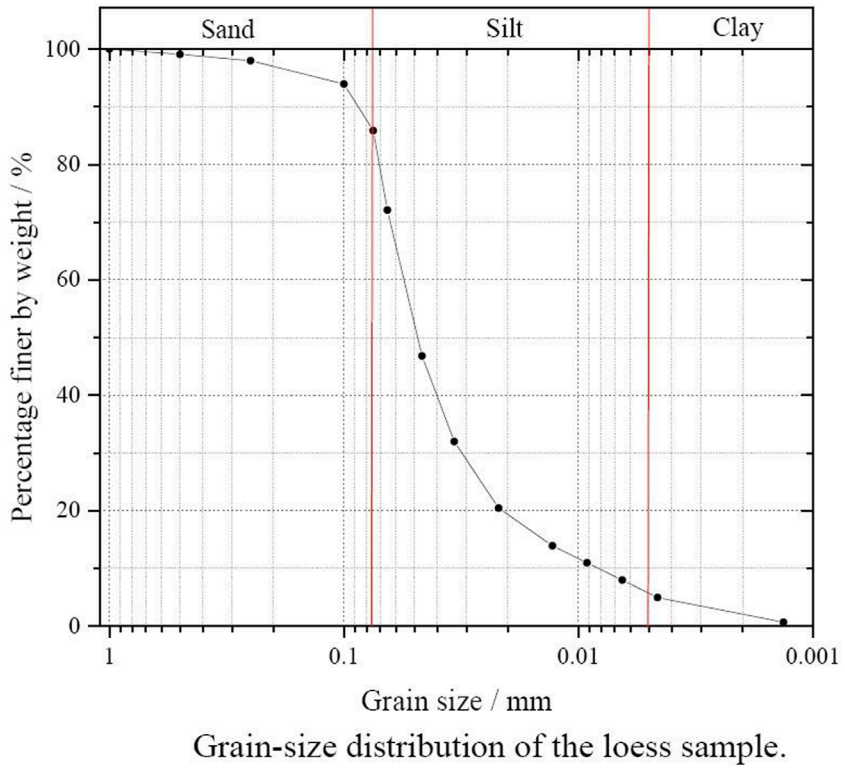

FIGURE 7
Grain-size distribution of YG-2.

4.3 Loess liquefaction test

Loess is a distinctive type of Quaternary deposit characterized by its porous microstructure, weak cohesion, high salt content, abundant silts, and large void spaces. When in an unsaturated state, it remains under-compacted (Lei, 1989; Qiang et al., 2013; Xie, 2001). These physical and structural properties render loess highly susceptible to water sensitivity and prone to seismic liquefaction, which are primary contributors to geological disasters such as subsidence and liquefaction.

In order to investigate whether liquefaction occurred in the landslide body during the earthquake, soil samples were extracted from two depths: 5 m at the main scarp and 15 m at the base of the landslide body (Figure 6). These samples underwent liquefaction tests using the WF-12440 dynamic triaxial torsional shear test system at the Key Laboratory of Loess Earthquake Engineering of the China Earthquake Administration.

Particle analysis showed that loess at a depth of 8 m at the flowslide site comprised 20.5% clay, 67.2% silt, and 12.3% sand, which was defined as clayish silt or sandy silt (Figure 7). The loess had a porous microstructure with weak cohesion. This kind of soil has high potential for liquefaction and vulnerability when it is saturated. Figure 7 shows the grain-size distribution of the loess, which consisted of about 7.96% clay, 77.90% silt, and 14.14% sand. All of the samples were Malan loesses formed in the Quaternary period (Q3). The physical parameters are shown in Table 2.

The test results indicated that preceding intermittent rainfall prior to the earthquake increased the slope's water content to 24.53%, thereby replenishing underground water sources. The sliding surface of the loess slope, situated 2–3 m above the red weathered sandstone, became saturated with underground water, while the upper layer of the slope approached saturation, creating conditions favorable for loess liquefaction due to elevated water content.

Testing of the YG-2 specimen revealed that the loess layer surrounding the sliding surface likely liquefied under dynamic loading of 25 kPa with 25 cycles. During this process, the pore water pressure ratio exceeded 0.2, causing a significant increase in dynamic strain amplitude to approximately 3%. Consequently, the liquefied loess layer transformed into a sliding surface, facilitating the downslope movement of the overburden loess deposit.

4.4 Analysis of slope hydrological conditions

According to the distribution of drainage springs, groundwater exploration in boreholes, and high-density electrical surveys, groundwater types on the Wamuhi hillslopes include water within the Quaternary aquifer's porous media and within fissures of Cretaceous sandstone. The topography of the bedrock interface plays a crucial role in controlling downslope flow at the hillslope scale (Burns et al., 1998; Freer et al., 2002). Six boreholes were strategically placed across the hillslope, with two of them (#32 and #33) yielding no groundwater (Figure 6). This suggests that the eastern boundary

TABLE 2 Physical index of soil samples.

Sample Number	Depth (m)	Density (g/cm^3)	Dry density (g/cm^3)	Water content (%)	Initial void ratio
YG-2	15	2.01	1.61	24.53	0.686
YG-3	5	1.4	1.35	4.04	1.007

of the aquifer lies between the Eastern and Western flow-slide sites. Groundwater was absent in the shallow loess of the Eastern landslide, while in the Western flowslide, the groundwater level was observed 2–3 m above the rock bed.

Four Electrical Resistivity Tomography (ERT) profiles were conducted using a Wenner-Schlumberger configuration. Profiles A–A and D–D were oriented E–W perpendicular to the sliding direction, while profiles B–B and C–C were oriented N–S along the first and second sliding directions of the Western flowslide, respectively. Apparent resistivity data were inverted using Res2dinv software based on the least-squares method (Loke and Barker, 1996).

Based on borehole data, mapping, and geological surveys, a digital elevation model of the bedrock interface was constructed. According to the ERT profiles (Figure 8), it was observed that water in Cretaceous sandstone fissures was more prevalent beneath the inferred bedrock interface, with the water table reaching depths below 18 m. Groundwater within the upper 15-m aquifers was dispersed and exhibited characteristics of upper backwater.

In the source area of the Western flowslide, discontinuous impermeable layers were found below the inferred bedrock interface, with backwater present in the loess layer. The inferred slip surface intersected the aquifer above the bedrock surface. Backwater emerged in depressions ahead of the source area, forming drainage springs (Figure 8). In the accumulation area, the impermeable layer beneath the bedrock surface was thicker, causing upper backwater to flow downslope into the Wamugou gully.

As shown in section A–A of Figure 8, water from sandstone fissures in the Eastern landslide was deeper, and no groundwater was detected in the loess layer above the inferred bedrock surface.

The second failure of the Western flowslide did not occur along the main sliding direction. Between boreholes 30 and 34, two drainage springs were observed, inducing saturated loess outcrops near the springs. One of these springs was situated midway along the main sliding path, while the other was located 50 m from the second flowslide crown. Along the direction of boreholes 30 and 34, which had the lowest slope gradient, several terrace edges collapsed and experienced retrogressive erosion more than in other directions, as observed from satellite imagery and terrain features. Additionally, the trajectory of the Wamugou gully aligned with the two failures at the Western flowslide. Thus, it is inferred that the process of groundwater transformation into streamflow and its control over micro-topography on the Wamuchi hillslope contributed to the landslide occurrence.

During rainfall and infiltration, the saturated zone above the bedrock thickened, causing intermittent saturated zones within bedrock depressions to connect, thereby enhancing lateral saturated flow downslope. This lateral flow continued until the saturated thickness above the bedrock diminished, leaving only depressions saturated. Consequently, changes in matric suction, suction stress, total unit weight, and effective stress occurred throughout the hillslope, reducing slope stability.

4.5 Terrain trend analysis and TWI calculation

In the study area located in the central region of Gansu Province, widespread distribution of Quaternary red soils with poor lithification overlays loess, forming typical loess slopes dominated by a combination of loess and red soils. Red soil acts as a relatively impermeable layer, with groundwater recharge entirely dependent on precipitation. Therefore, based on the 12.5-m resolution DEM prior to the earthquake, we extracted 100 elevation points from landslides located in the east and west for terrain trend analysis (Figure 9) and calculated the TWI values for the entire study area (Figure 10). This enabled us to assess the rainfall runoff conditions at the landslides before the earthquake and to identify areas within the study region that were most affected by rainfall.

Figure 9A indicates that prior to the earthquake, the overall terrain trend of the western landslide was characterized by a lower central area and higher sides. Consequently, following rainfall, a significant amount of water would accumulate at the landslide location towards the right of the center, resulting in substantial groundwater recharge. In contrast, Figure 9B shows that the original terrain trend of the eastern landslide had a higher central area with lower sides. Therefore, after rainfall, most of the water would flow down the slope rather than causing significant infiltration.

Figure 10 illustrates that areas with lower pre-landslide Topographic Wetness Index (TWI) values in Yongguang Village are predominantly concentrated in the eastern, western, and southwestern parts of the study area, including within the western landslide area. Conversely, the eastern landslide area exhibits higher TWI values. Therefore, prior to the landslide, the western landslide location was identified as an area more susceptible to terrain influence and significant rainfall impact compared to the eastern landslide area.

4.6 Effect of site conditions on ground motion of the hillslope

The characteristics of ground motion at a specific site are primarily influenced by three factors: the seismic source, the propagation path, and local geological and topographical features. In this study, the landslide occurred only 20 m from the main Hetuo fault (Figure 2). Given its proximity, the location of the landslide was pivotal in its occurrence.

Following the earthquake, extensive investigations were conducted to analyze the distribution pattern of coseismic landslides

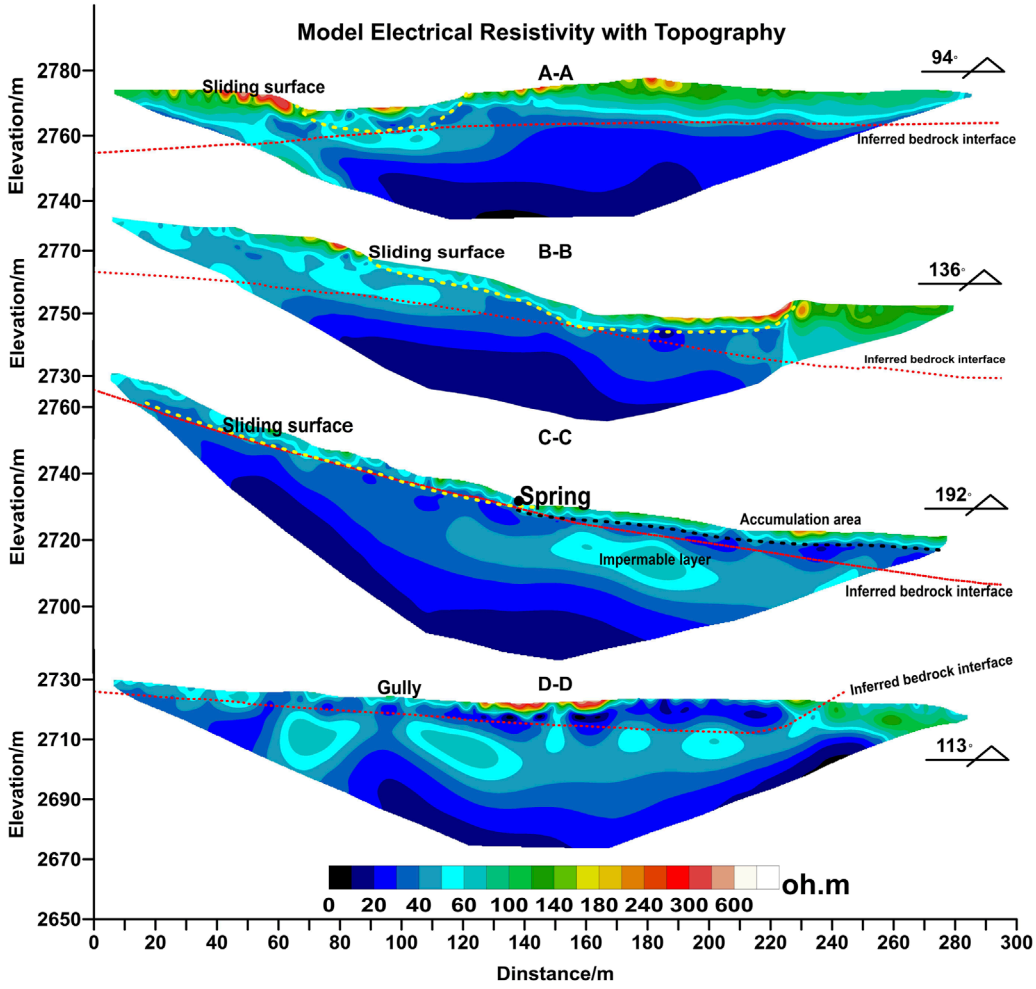

FIGURE 8
Electrical resistivity tomography results: location of profile.

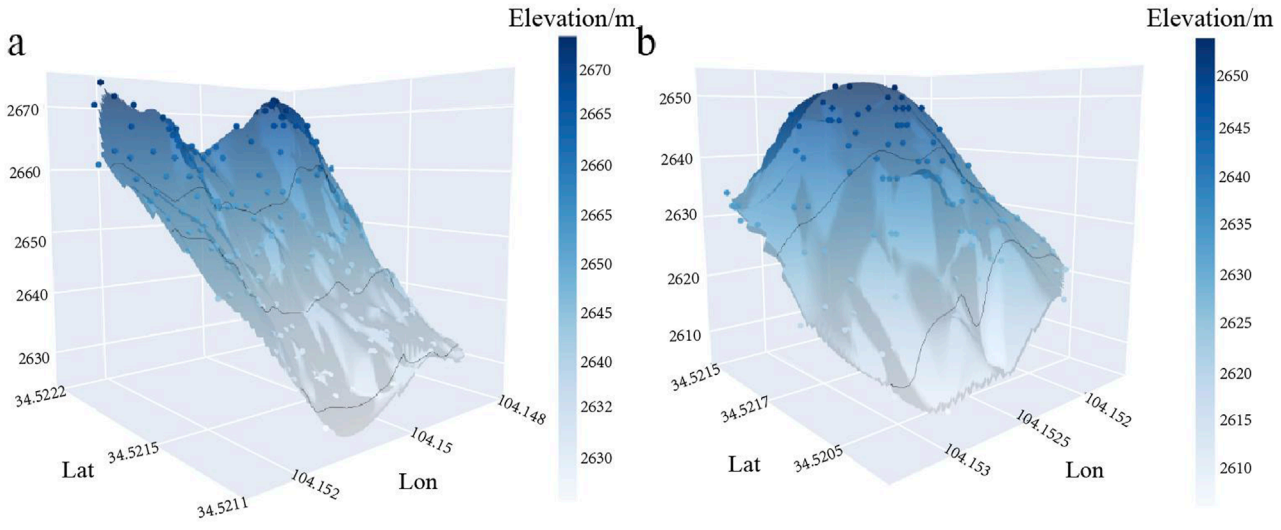

FIGURE 9
Pre-Landslide Terrain Trend Map: **(A)** Terrain trend of the western landslide **(B)** Terrain trend of the eastern Landslide.

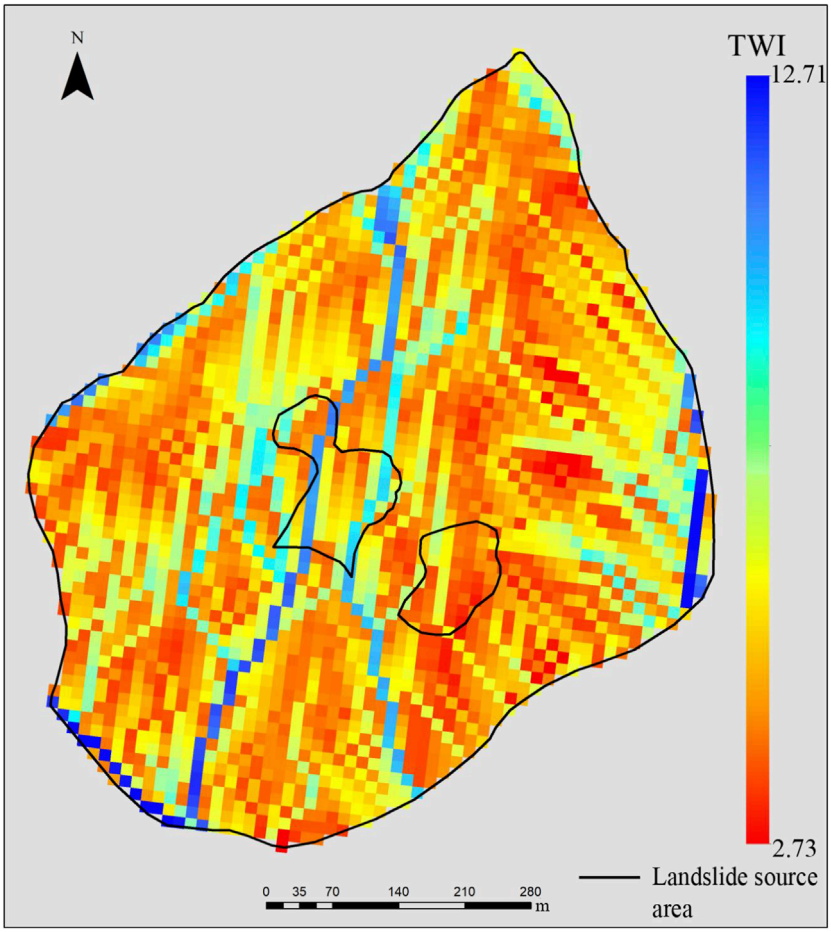

FIGURE 10
Pre-landslide distribution map of topographic wetness index (TWI).

relative to the seismogenic fault, which did not produce surface rupture. The Wamuchi landslide occurred on the hanging wall of the Hetuo fault, suggesting it was subjected to significant ground shaking during the earthquake.

The Earth's surface is inherently uneven, featuring irregularities such as mountains, canyons, and other concave features that can alter the propagation of surface waves (Ma et al., 2007). Topographic amplification of ground acceleration occurs when seismic waves entering the base of a topographic ridge are reflected back into the rock mass and diffracted along the free surface. This phenomenon leads to a concentration of seismic energy towards ridge crests, resulting in heightened ground acceleration through constructive interference of reflections and diffractions (Bouchon, 1973; Davis and West, 1973; Geli et al., 1988).

Huang et al. (2013) compiled strong motion recordings from the main shock and significant aftershocks of the M-Z earthquake, as observed by the National Strong Motion Observation Network System (NSMONS) of China. These recordings revealed that the highest Peak Ground Acceleration (PGA) during the main shock was recorded at the Minxian Station, reaching 178 Gal. Moreover, PGAs were notably higher on the hanging wall of faults. Therefore, the combination of the landslide's proximity to the fault and its position on the hanging wall were significant factors contributing to the landslide occurrence.

Additionally, basin effects, near-fault effects, and topographic amplification all played roles in intensifying ground shaking, which ultimately triggered the landslide.

4.7 Slideway terrain control flow-sliding features

Displaced soils from the Eastern and Western slopes flowed with different slip distance and flow-sliding features, which mainly depended on the physical and mechanical properties of the failure mass, rush-out velocity, and terrain characteristics of slideways.

In the analysis of landside mobility, the concept of travel angle (Áa) has been used widely (Qiu et al., 2017; Scheidegger, 1973), where tan (Áa) = H/L (H is the height of the landslide, i.e., the difference in elevation between its crown and tip, and L is its horizontal distance). Áa is also known as the apparent friction angle, and its low vlue corresponds to high mobility. The apparent friction angles of the Western and Eastern landslide were 0.9 and 1.2, respectively. The water content of displaced soils on the Western

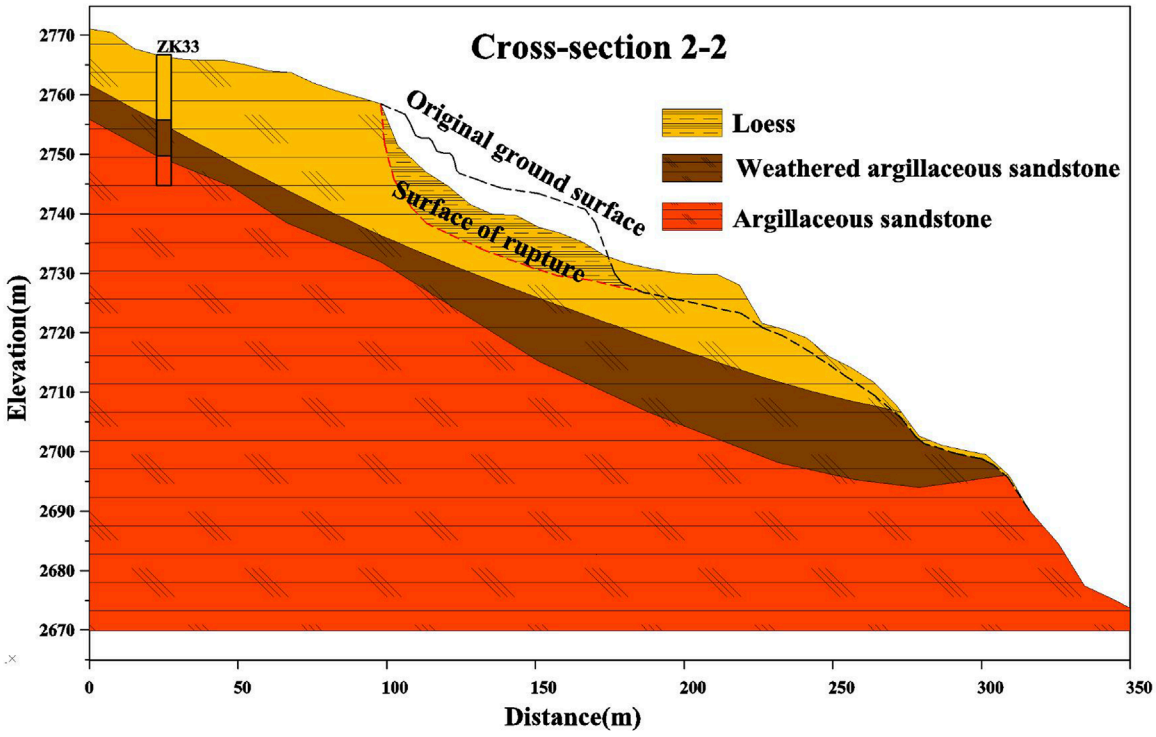

FIGURE 11
The geological profile of the Eastern landslide.

slope was obviously higher than that on the Eastern slope. The higher the water content was, the lower the strength and the stronger the mobility of the displaced loess.

At present, the Scheidegor approach is the most commonly used for estimating the velocity of a landslide. The formula is shown in Equation 4:

$$V = \sqrt{2g(H - fL)} \tag{4}$$

where V is the landslide velocity (m/s); g is the gravitational acceleration (m/s2); H (m) is the height difference between the top point of the landslide rear edge and the calculated point; L (m) is the horizontal distance from the top point to the calculated point along the sliding direction; and f is the equivalent friction factor with a value 0.84 (i.e., the vertical height difference of 182 m divided by the horizontal distance of 1.1 km). According to the longitudinal profile of the Eastern and Western flowslides (Figures 11, 12), the horizontal distance and height difference of the estimated landslide points was determined. Then, we calculated the velocity of the landslide from the starting to the final stoppage.

The characteristics of the flowslide differed significantly between the Eastern and Western slopes of the Wamuchi hillslope. In the source area of the Western flowslide, the slope was gentle, allowing for a longer accelerating distance before entering the slideway compared to the Eastern landslide. This longer acceleration distance resulted in a higher rush-out velocity for the displaced mass, which entered the slideway with greater initial speed.

The slideway of the Western slope followed the long and narrow Wamugou gully, which featured flowing water. The narrow width of the gully and the presence of water contributed to the cohesive strength of the soil mass along the slideway. The gentle slope and soft soil conditions along the gully facilitated the maintenance of higher flow-sliding velocities for the displaced loess.

Conversely, the slideway of the Eastern slope followed the steep main scarp of an old landslide, characterized by a weathered sandstone outcrop. This slideway was broader, approximately 20 m wide, and protruded like a ridge in the middle. These three factors—the slope gradient, presence of water flow, and topographic features—contributed to distinct flow-sliding characteristics between the Eastern and Western flowslides.

4.8 Instability mechanism of the two landslides at the wamuchi hillslope

Cascini et al. (2010) classified shallow landslides based on their stages of failure. The failure stage is defined as the formation of a continuous shear surface through the entire soil mass. The post-failure stage is represented by the rapid generation of large plastic strains and the consequent sudden acceleration of the failed soil mass. Based on the acceleration of the failed mass, rainfall-induced shallow landslides can be classified as slide, slide to flow, and flowslide. The eventual sudden acceleration of the displaced mass in the post-failure stage is a consequence of the slope instability process; therefore, the failure and post-failure stages should be analyzed separately (Zhang et al., 2011). Meunier et al. (2008) mentioned that these changes may be sufficient to cause a failure.

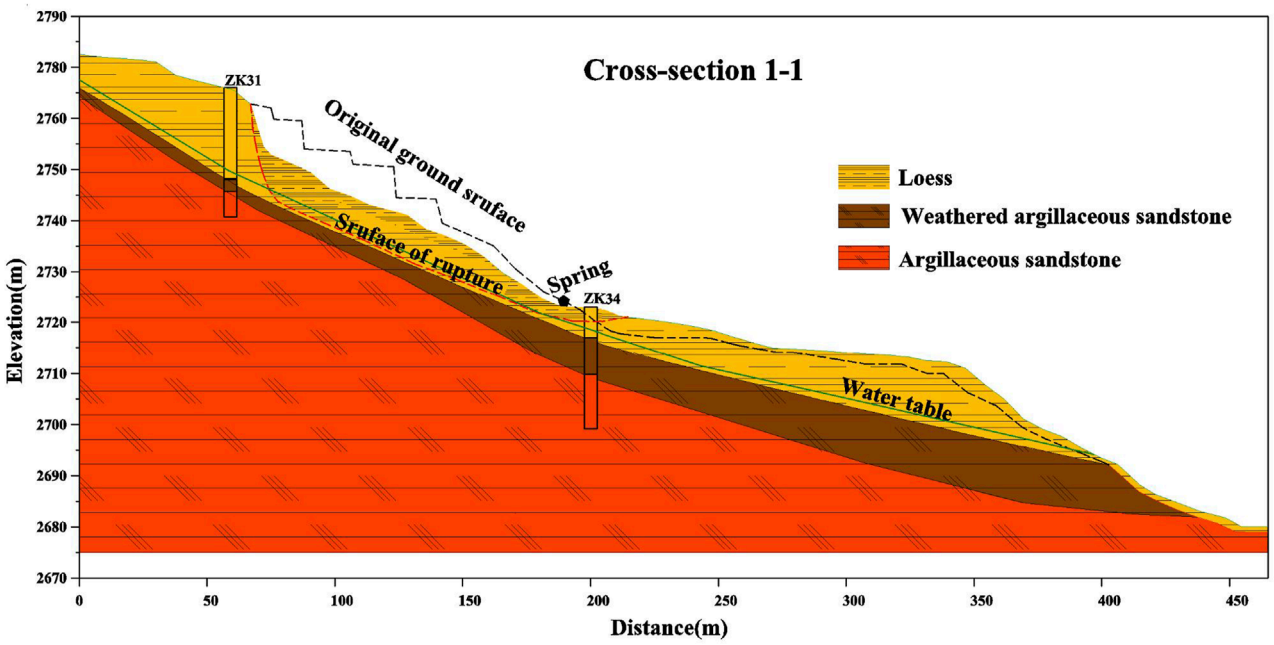

FIGURE 12
The geological profile of the Western flowslide.

The failure mechanism of the Wamuchi flowslides could also be separated by the instability mechanism and flow-sliding mechanism.

Hillslope failure occurs when the shear stress across a potential failure plane exceeds the substrate strength. Earthquakes affect the stability of slopes in two ways. First, the ground shaking may reduce the frictional strength of the subsoil by shattering the soil mass or causing liquefaction of saturated soils. Second, the seismic acceleration may result in short-lived and episodic changes of the normal (tensile) and shear stresses in the slopes during earthquakes. The failure mechanism of the Wamuchi hillslope could be explained by these two concepts.The role of water and topography in this process cannot be overlooked. According to the analysis of topographic trends in Section 4.5, the western landslide occurred in a concave terrain, which facilitates the collection and infiltration of precipitation. The Topographic Wetness Index (TWI) for the western landslide also indicates that the region has a larger slope area, making it a potential zone for increased soil moisture and water accumulation.

4.8.1 The eastern landslide

The Eastern landslide occurred on a convex hillslope (Figure 11) bounded by gullies (Figure 6). Strong ground motion, amplified by basin effects and topographic amplification, caused significant shattering of the Quaternary loess. Additionally, antecedent intermittent rainfall played a crucial role in slope stability, as rain infiltration into the shallow loess layer reduced negative pore water pressure. The combined effects of intense ground motion and rainfall infiltration significantly weakened the strength of the substrate.

Moreover, the topographic gradient of the Eastern slope increased due to the undercutting by an old landslide on the southern and eastern sides of the Wamuchi slope. This gradient increase altered the slope's stress field, contributing further to its instability. These factors collectively controlled the occurrence of instability on the Eastern slope.

4.8.2 The western flowslide

Special terrain and hydrological conditions influenced the groundwater table position (Figure 12) and played a crucial role in determining the location of the Western flowslide. Prior to the earthquake, prolonged rainfall increased the water content of the Wamuchi slope significantly, reaching 24.53%. This moisture infiltration saturated the sliding surface of the loess slope at depths of 2–3 m above the sandstone, with the upper layers also partially saturated. These conditions were conducive to loess liquefaction.

Based on test results, the slope underwent complete liquefaction under saturated conditions when subjected to ground motions with a Peak Ground Acceleration (PGA) of 200 Gal or greater. Considering the ground motion attenuation relationship and records from the Minxian seismic station (PGA = 178 Gal), it was determined that the ground motion exceeded 200 Gal PGA at the Wamuchi hillslope during the Minxian earthquake. This seismic loading induced excess pore-water pressure within the shearing soil, ultimately causing the failure of the Western slope.

4.9 Flow-sliding mechanism of displaced loess

Under the combined influence of the earthquake and antecedent rainfall, both the Western and Eastern slopes sequentially entered

instability stages. Based on our field investigation, the two flowslides located within 30 m of each other exhibited distinct sliding characteristics. The properties of the displaced loess mass, initial velocity, and the nature of the flowing channel played significant roles in determining flow-sliding distance, mean velocity, and thrusting.

Residual strength is a critical parameter in assessing the stability of loess deposits affected by liquefaction. Generally, residual strength decreases with higher degrees of saturation and increased void ratios (Pei et al., 2017). The instability mechanisms altered the physical properties of the displaced loess. Additionally, groundwater conditions leading to liquefaction of the Western slope resulted in higher water content and mobility compared to the shattered loess of the Eastern slope. Moreover, the initial velocity was influenced by the sliding distance under similar acceleration conditions.

The Western flowslide utilized an optimal gully as its flowing channel, maintaining a consistent width that allowed for a steady flow velocity. In contrast, the Eastern landslide followed the channel of an old landslide, which was steeper by 20 m compared to the Western channel. This Eastern channel was situated in red sandstone with higher surface friction, unlike the Western channel covered by saturated and softened weathered sandstone and loess deposits. These factors collectively controlled the flow distance of the two landslides.

5 Conclusion

Landslides and flowslides are the main forms of failure of aeolian loesses at intermountain slopes under external forces including earthquakes and rainfall. Two flowslides induced by the M-Z earthquake (Mw = 5.9) in 2013, located within 100 m of each other, occurred at the same hillslope with different flow-sliding features. The sliding distance of the Western flowslide was about 1.17 km, and showed a mud flow pattern, whereas that of the Eastern landslide was only 0.35 km. Based on UAV photogrammetry, a field survey, a laboratory test, geophysical exploration, and data analysis, we investigated the slope morphology, physical and mechanical properties of the loess, strata, hydrogeological conditions, historical geological hazards, ground motion, and rainfall before the earthquake was carried out to determine the failure characteristics of two flowslides. The triggering mechanism and controlling factor were analyzed comparatively. The results of our research are summarized below.

(1) The aeolian loess intermountain area had loose and strong structural characteristics, and it was prone to loess geological disasters. The argillaceous sandstone beneath the Wamuchi slope was severely weathered and featured abundant fissure water in the rock mass. Several drainage springs were spread all over the hillslope ground, one of which was located at the source area of the Western flowslide. Old landslides with weathered argillaceous sandstone outcrops developed along the gully sides around the flowslide site. Those at the eastern and front edges of the Eastern flow-sliding slope were cut by the head scrape of the old landslide, forming solitary, convex, and steep terrain, which greatly reduced the stability of the slope.

(2) The Wamuchi hillslope was located on the intermontane colluvial fan in Neogene basin. The special topography and loose loess induced an obvious ground motion amplification effect. In addition, the surface trace of the M-Z earthquake seismogenic fault passed through the front of the Wamuchi hillslope, and the flowslide site was located on the hanging wall. The fault-hanging wall effect and the near-field effect of the earthquake induced strong ground shaking on the slope. Ground motion was the main reason for the instability of the Loess slope.

(3) The 20-day cumulative rainfall before the earthquake was higher than the local mean monthly cumulative rainfall in July over the past 20 years. Rainfall increased the water content of the slope soil and decreased the matrix suction of the unsaturated loess and shear strength, which led to a decrease in slope stability. Pre-earthquake terrain trend analysis of the study area indicates that the western landslide features a concave topography, whereas the eastern landslide exhibits a convex topography. The TWI prior to the landslide indicates that the western landslide area has a larger contributing area of slope, making it a potential region for increased soil moisture and water accumulation. Therefore, this area is more susceptible to the influence of regional topography.

(4) According to the distribution of drainage springs and groundwater exploration in boreholes on the slopes, the eastern boundary of groundwater lay between the Eastern and Western flow-sliding sites. There was no groundwater in the shallow loess of the Eastern landslide, whereas the groundwater level of the Western flowslide was 2–3 m above the rock bed. The loess on the sliding surface of the Western flowslide was saturated. Stability in the Western slope was lower than that of the Eastern slope.

(5) Strong ground shaking induced loess liquefaction on the Western slope. High pore pressure led to an obvious blasting phenomenon, and the displaced soil was instantaneously transformed into loess debris. The Eastern slope, with a lower stability, was shattered by strong motion, and the shallow soil was instantaneously broken into loess debris.

(6) Displaced soils from the Eastern and Western slopes flowed with different slip distances and flow-sliding features, which mainly owed to the physical and mechanical properties of the failure mass, rush-out velocity, and terrain characteristics of the slideways.

Data availability statement

The raw data supporting the conclusions of this article will be made available by the authors, without undue reservation.

Author contributions

KL: Methodology, Software, Writing–original draft. LW: Project administration, Resources, Writing–review and

editing. JS: Investigation, Methodology, Writing–original draft. SX: Investigation, Writing–original draft. YL: Investigation, Writing–original draft. WT: Investigation, Writing–original draft. FL: Methodology, Software, Writing–original draft.

Funding

The author(s) declare that financial support was received for the research, authorship, and/or publication of this article. This work was funded by Central Public-interest Scientific Institution Basal Research Fund (2019IESLZ04); The Science for Earthquake Resilience of China Earthquake Administration (XH24043A); 2024 Longyuan Young Talent Projects for Innovation and Entrepreneurship (2024QNTD51).

Acknowledgments

We thank Xingwang Liu and Yanxiu Shao for his providing of some geological data associated with the research region.

Conflict of interest

The authors declare that the research was conducted in the absence of any commercial or financial relationships that could be construed as a potential conflict of interest.

Generative AI statement

The author(s) declare that no Generative AI was used in the creation of this manuscript.

Publisher's note

References

Beven, K. J., and Kirkby, M. J. (1979). A physically based, variable contributing area model of basin hydrology/Un modèle à base physique de zone d'appel variable de l'hydrologie du bassin versant. *Hydrological Sci. J.* 24 (1), 43–69. doi:10.1080/02626667909491834

Bouchon, M. (1973). Effect of topography on surface motion. *Bull. Seismol. Soc. Am.* 63, 615–632. doi:10.1785/bssa0630020615

Burns, D. A., Hooper, R. P., McDonnell, J. J., Freer, J. E., Kendall, C., and Beven, K. (1998). Base cation concentrations in subsurface flow from a forested hillslope: the role of flushing frequency. *Water Resour. Res.* 34, 3535–3544. doi:10.1029/98WR02450

Cascini, L., Calvello, M., and Grimaldi, G. M. (2010). Groundwater modeling for the analysis of active slow-moving landslides. *J. Geotech. Geoenvironmental Eng.* 136, 1220–1230. doi:10.1061/(ASCE)GT.1943-5606.0000323

Che, A., Wu, Z., and Lei, T. (2013). Surface wave investigation and dynamic stability analysis for earthquake-induced loess landslides. *China Earthq. Eng. J.* 724–729. doi:10.3969/j.issn.1000-0844.2013.04.002

Chen, L., Wang, Y., Yuan, X., Li, Z., Wang, Y., Nie, G., et al. (2024). Preliminary analysis for the triggering of soil flowslide that occurred in Zhongchuan Town following the 2023 Jishishan MS6.2 earthquake in Gansu Province. *J. Earthq. Eng. Eng. Vib.* 44, 187–193. doi:10.13197/j.eeed.2024.0118

Davis, L. L., and West, L. R. (1973). Observed effects of topography on ground motion. *Bull. Seismol. Soc. Am.* 63, 283–298. doi:10.1785/bssa0630010283

Freer, J., McDonnell, J. J., Beven, K. J., Peters, N. E., Burns, D. A., Hooper, R. P., et al. (2002). The role of bedrock topography on subsurface storm flow. *Water Resour. Res.* 38, 1269. doi:10.1029/2001WR000872

Geli, L., Bard, P.-Y., and Jullien, B. (1988). The effect of topography on earthquake ground motion: a review and new results. *Bull. Seismol. Soc. Am.* 78, 42–63. doi:10.1785/bssa0780010042

He, W., Zheng, W., and Wang, A. (2013). New activities of lintan-dangchang Fault and its relations to minxian-zhangxian MS6.6 earthquake. China earthq. *Eng. J.* 32, 751–760. doi:10.3969/j.issn.1000-0844.2013.04.751

Huang, X., Wen, R., Ren, Y., and Xu, P. (2013). Strong mmotion records and its characteristics in minxian-zhangxian Ms6.6 earthquake on july 22,2013. *China Earthq. Eng. J.*, 489–496. doi:10.3969/j.issn.1000-0844.2013.03.0489

Hungr, O., Evans, S. G., Bovis, M. J., and Hutchinson, J. N. (2001). A review of the classification of landslides of the flow type. *Environ. Eng. Geosci.* 7, 221–238. doi:10.2113/gseegeosci.7.3.221

Lei, X. (1989). The relations between microfabrics of loess and paleoclimate in China. *Geol. Rev.* 35, 333–341. doi:10.16509/j.georeview.1989.04.007

Li, L., Wu, Z., Li, R., and Zhao, T. (2018). Survey of overburden thickness of sites and establishment of three-dimensional terrain model in the meizoseismal area of minxian—zhangxian M S 6.6 earthquake. *China Earthq. Eng. J.* 40, 1191–1197. doi:10.3969/j.issn.1000-0844.2018.06.1191

Loke, M. H., and Barker, R. D. (1996). Rapid least-squares inversion of apparent resistivity pseudosections by a quasi-Newton method. *Geophys. Prospect.* 44, 131–152. doi:10.1111/j.1365-2478.1996.tb00142.x

Lu, F. C., Liu, K., Xu, S. H., Zhang, J. Y., and Guo, D. N. (2024a). Analysis of the differences between two landslides on one slope in Yongguang village based on physical models and groundwater identification. *Water* 16 (24), 3591. doi:10.3390/w16243591

Lu, F. C., Liu, K., Xu, S. H., Zhang, J. Y., Tian, W. T., and Guo, D. N. (2024b). Study on the influence of shallow groundwater and hydrological processes on loess liquefaction and mud flow sites. *J. Eng. Geol.* doi:10.13544/j.cnki.jeg.2024-0099

Ma, P., and Peng, J. (2022). On loess geohazards chain(1). *J. Nat. Disasters* 31 (2), 1–11. doi:10.13577/j.jnd.2022.0201

Ma, S., Archuleta, R. J., and Page, M. T. (2007). Effects of large-scale surface topography on ground motions, as demonstrated by a study of the san gabriel mountains, Los Angeles, California. *Bull. Seismol. Soc. Am.* 97, 2066–2079. doi:10.1785/0120070040

Meunier, P., Hovius, N., and Haines, J. A. (2008). Topographic site effects and the location of earthquake induced landslides. *Earth Planet. Sci. Lett.* 275, 221–232. doi:10.1016/j.epsl.2008.07.020

Pei, X., Zhang, X., Guo, B., Wang, G., and Zhang, F. (2017). Experimental case study of seismically induced loess liquefaction and landslide. *Eng. Geol.* 223, 23–30. doi:10.1016/j.enggeo.2017.03.016

Qiang, W., Junjie, S., Lanmin, W., and Xiuqing, C. (2013). Review and discussion on seismic subsidence of loess. Earthq. *Res. China* 27, 479–489.

Qiu, H., Cui, P., Regmi, A. D., Hu, S., Wang, X., Zhang, Y., et al. (2017). Influence of topography and volume on mobility of loess slides within different slip surfaces. *CATENA* 157, 180–188. doi:10.1016/j.catena.2017.05.026

Scheidegger, A. E. (1973). On the prediction of the reach and velocity of catastrophic landslides. *Rock Mech. Felsmech. M. Canique Roches* 5, 231–236. doi:10.1007/BF01301796

Tian, X., Li, Z., and Xu, Q. (2013). The strong motion records and preliminary analysis for minxian-zhangxian M6.6 earthquake in Gansu province. *China Earthq. Eng. J.*, 497–502. doi:10.3969/j.issn.1000-0844.2013.03.0497

Varnes, D. J. (1958). Landslide types and processes. *Landslides and engineering practice* 24, 20–47.

Wang, A., and Liu, F. (2013). Estimation of peak ground acceleration in magistoseismic area of the minxian-zhangxian Ms6.6 earthquake. *China Earthq. Eng. J.*, 483–488. doi:10.3969/j.issn.1000-0844.2013.03.0483

Wang, L., Chai, S., Bo, J., Wang, P., Xu, S., Li, X., et al. (2023). Triggering types, characteristics and disaster mechanism of seismic loess landslides. *Chin. J. Geotechnical Eng.* 45 (8), 1543–1554. doi:10.11779/CJGE20220531

Wang, L., and Wu, Z. (2014). Earthquake damage characteristics of the Minxian–Zhangxian Ms6.6 earthquake and its lessons. *China Earthq. Eng. J.* 35, 401–412. doi:10.3969/i.issn.1002-8412.2014.03.024

Wang, L., Xie, H., Pu, X., Li, Z., Guo, X., and Yao, Y. (2024). Sliding process and causative mechanism of the Zhongchuan landslide-mudflow disaster chain induced by the 2023Jishishan M_S6.2 earthquake. *China Earthq. Eng. J.* 46 (4), 791–801.

Wang, L. M., Wang, Q., Wu, Z. J., and Che, A. L. (2017a). "Loessial landslides induced by the minxian–zhangxian Ms6.6 earthquake of China in 2013," in *Geotechnical hazards from large earthquakes and heavy rainfalls* (Tokyo: Springer), 183–192. doi:10.1007/978-4-431-56205-4_17

Wang, Q., Wang, L., Wang, J., and Guo, P. (2017b). Prediction of loess earthquake geological disasters in the reconstruction sites after the Minxian-Zhangxian Ms 6.6 earthquake. *Hydrogeol. Eng. Geol.* 44, 137–142. doi:10.16030/j.cnki.issn.1000-3665.2017.05.21

Wang, Q., Wang, Z. M., Su, Y. Q., Zhong, X. M., Wang, L. M., Ma, H. P., et al. (2021). Characteristics and mechanism of the landslide in Yongguang village, minxian county, China. *Nat. Hazards* 105 (2), 1413–1438. doi:10.1007/s11069-020-04360-7

Wang, S. (2014). Cause analysis of extremely heavy hail flood and debris flow disaster in minxian county, Gansu province. *Water Resour.*, 22–23. doi:10.3969/j.issn.1672-2469.2014.09.007

Xie, D. (2001). Exploration of some new tendencies in research of loess soil mechanics. *Chin. J. Geotech. Eng.* 23, 3–13. doi:10.3321/j.issn:1000-4548.2001.01.002

Xu, C., Xu, X., Zheng, W., Min, W., Ren, Z., and Li, Z. (2013). Landslides triggered by the 2013MInxian-Zhangxian, Gansu province Ms6.6 earthquake and its tectonic analysis. *Seismol. Geol.* 35, 616–626. doi:10.3969/j.issn.0253-4967.2013.03.015

Xu, Q., Peng, D. L., Fan, X. M., Dong, X., Zhang, X., Wang, X., et al. (2024). Preliminary study on the characteristics and initiation mechanism of Zhongchuan Town flowslide triggered by Jishishan Ms 6.2 earthquake in Gansu Province. *Geomatics Inf. Sci. Wuhan Univ.* doi:10.13203/J.whugis20240007

Xu, S., and Sun, J. (2013). Study of the characteristics and inducing mechanism of typical earthquake landslides of the Minxian–Zhangxian Ms6.6 earthquake. *China Earthq. Eng. J.* 35, 471–476. doi:10.3969/j.issn.1000-0844.2013.03.0471

Yan, W., Wu, Z., and Che, A. (2013). Microtremor measurement research of amplification effect in the loess site of the MinXian-ZhangXian Ms6.6 earthquake. *China Earthq. Eng. J.*, 477–482. doi:10.3969/j.issn.1000-0844.2013.03.0477

Zhang, L. L., Zhang, J., Zhang, L. M., and Tang, W. H. (2011). Stability analysis of rainfall-induced slope failure: a review. *Proc. Inst. Civ. Eng. - Geotech. Eng.* 164, 299–316. doi:10.1680/geng.2011.164.5.299

Zheng, W., Yuan, D., and He, W. (2013). Geometric pattern and active tectonics in Southeastern Gansu province:Discussion on seismogenic mechanism of the Minxian-Zhangxian Ms6.6 earthquake on July 22,2013. *Chin. J. Geophys.* 56, 4058–4071. doi:10.6038/cjg20131211